



HAL
open science

Size Dependence of Lattice Parameter and Electronic Structure in CeO₂ Nanoparticles

Damien Prieur, Walter Bonani, Karin Popa, Olaf Walter, Kyle W. Kriegsman, Mark H. Engelhard, Xiaofeng Guo, Rachel Eloirdi, Thomas Gouder, Aaron Beck, et al.

► **To cite this version:**

Damien Prieur, Walter Bonani, Karin Popa, Olaf Walter, Kyle W. Kriegsman, et al.. Size Dependence of Lattice Parameter and Electronic Structure in CeO₂ Nanoparticles. *Inorganic Chemistry*, 2020, 59 (8), pp.5760-5767. 10.1021/acs.inorgchem.0c00506 . cea-03593552

HAL Id: cea-03593552

<https://cea.hal.science/cea-03593552>

Submitted on 2 Mar 2022

HAL is a multi-disciplinary open access archive for the deposit and dissemination of scientific research documents, whether they are published or not. The documents may come from teaching and research institutions in France or abroad, or from public or private research centers.

L'archive ouverte pluridisciplinaire **HAL**, est destinée au dépôt et à la diffusion de documents scientifiques de niveau recherche, publiés ou non, émanant des établissements d'enseignement et de recherche français ou étrangers, des laboratoires publics ou privés.



Distributed under a Creative Commons Attribution 4.0 International License

Size Dependence of Lattice Parameter and Electronic Structure in CeO₂ Nanoparticles

Damien Prieur,* Walter Bonani,* Karin Popa, Olaf Walter, Kyle W. Kriegsman, Mark H. Engelhard, Xiaofeng Guo, Rachel Eloirdi, Thomas Gouder, Aaron Beck, Tonya Vitova, Andreas C. Scheinost, Kristina Kvashnina, and Philippe Martin

Cite This: *Inorg. Chem.* 2020, 59, 5760–5767

Read Online

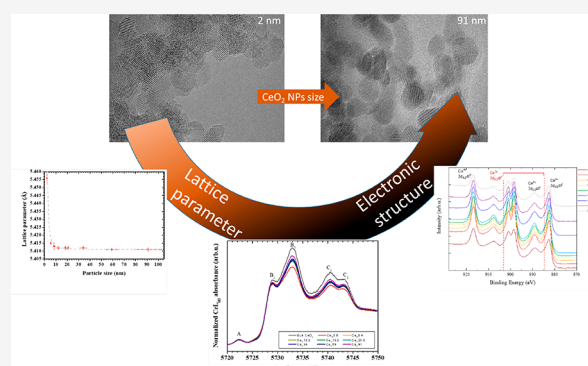
ACCESS |

Metrics & More

Article Recommendations

Supporting Information

ABSTRACT: Intrinsic properties of a compound (e.g., electronic structure, crystallographic structure, optical and magnetic properties) define notably its chemical and physical behavior. In the case of nanomaterials, these fundamental properties depend on the occurrence of quantum mechanical size effects and on the considerable increase of the surface to bulk ratio. Here, we explore the size dependence of both crystal and electronic properties of CeO₂ nanoparticles (NPs) with different sizes by state-of-the-art spectroscopic techniques. X-ray diffraction, X-ray photoelectron spectroscopy, and high-energy resolution fluorescence-detection hard X-ray absorption near-edge structure (HERFD-XANES) spectroscopy demonstrate that the as-synthesized NPs crystallize in the fluorite structure and they are predominantly composed of Ce^{IV} ions. The strong dependence of the lattice parameter with the NPs size was attributed to the presence of adsorbed species at the NPs surface thanks to Fourier transform infrared spectroscopy and thermogravimetric analysis measurements. In addition, the size dependence of the t_{2g} states in the Ce L_{III} XANES spectra was experimentally observed by HERFD-XANES and confirmed by theoretical calculations.



INTRODUCTION

CeO₂-based nanoparticles (NPs) offer unique redox properties that open promising possibilities for applications in catalysis,^{1,2} energy storage,^{3,4} biomedicine,⁵ and nuclear activities.⁶ Quantum mechanical size effects, combined with a considerable increase of the surface to bulk ratio, are responsible for the unique properties of nanometer-sized particles, including electronic and geometric structure, and optical and magnetic properties.^{7,8} A thorough understanding of the dependence of these properties on particle size is of great importance notably for the design of next generation materials.

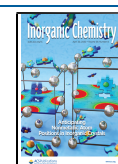
In this context, our work focuses on studying the size dependence of both crystallographic and electronic structures of CeO₂ NPs, as these two fundamental properties are of technological importance and theoretical interest and broad prospects.² The change of unit cell dimensions with decreasing particle size has been previously reported, but remains a subject of discussion. Different hypotheses have been put forward to explain this phenomenon: surface stress induced by the presence of sorbed species and partial reduction of Ce^{IV} to Ce^{III}.^{9–11} Furthermore, the electronic structure and its size dependence is of fundamental interest as energetic and catalytic properties notably lie on it.²

In the present work, the crystal structure of as-synthesized CeO₂ NPs was characterized by using X-ray diffraction (XRD)

and transmission electron microscopy (TEM) giving access to their size and lattice parameter. Fourier transform infrared spectroscopy (FTIR) and thermogravimetric analysis (TGA) was performed to determine species potentially adsorbed at the surface. Furthermore, we probed the electronic structure of CeO₂ NPs using both high-resolution X-ray photoelectron spectroscopy (XPS) and high-energy resolution fluorescence-detection hard X-ray absorption near-edge structure (HERFD-XANES) spectroscopy at the Ce L_{III} edge. Thanks to the use of an X-ray emission spectrometer, such inner-shell spectroscopy provides an element-selective probe of the electronic state and allows observing spectral features with significantly enhanced energy resolution compared to usual data limited by Ce L_{III} edge core hole lifetime broadening (Supporting Information Figure S1).^{12,13}

Received: February 21, 2020

Published: April 1, 2020



■ EXPERIMENTAL METHODS

Please note that a careful attention should be made for the characterization of these NPs material to avoid any energy-induced transformations.

Synthesis Methods. Nanoparticles Obtained by Hydrothermal Treatment. Ceria NPs samples were synthesized by alkaline precipitation of cerium ammonium sulfate precursor followed by hydrothermal condensation in a pressurized autoclave at different temperatures.^{14,15} In detail, a 1 M Ce(IV) solution was prepared by dissolving cerium(IV) ammonium sulfate dehydrate (Alfa Aesar) in deionized water; cerium(IV) hydroxide was directly precipitated by adding an excess of ammonium hydroxide (Sigma-Aldrich, 25% in water) under constant stirring for 3 h. A yellow cerium(IV) hydroxide precipitate was recovered by centrifugation, repeatedly washed with deionized water, and hydrothermally treated in a stainless steel reactor vessel with Teflon insert (total free volume 12 mL). Typically, 200 mg of cerium(IV) hydroxide was suspended in 10 mL of deionized water and heated for 3 h under autogenous pressure at different temperatures. After cooling, the solid residue was recovered, washed with deionized water, dehydrated with ethanol and acetone, and dried overnight in a chemical fume hood. The resulting dry powders were analyzed by XRD with a Rigaku Miniflex 600 diffractometer. The crystallite size of the nanopowders was estimated from the XRD pattern using the Scherrer equation and averaging the results of 8 selected peaks in the 2θ range between 25 and 80°. Nanoparticle samples obtained by hydrothermal condensation at 150, 180, and 200 °C were labeled as Ce_2, Ce_4.2, and Ce_5.6, giving their respective crystallite size in nanometer.

Nanoparticles Obtained by Thermal Treatment in Dry Conditions. In order to obtain samples with larger crystallites size, the dry powder samples obtained by hydrothermal treatment were calcined for 1 h at temperatures ranging from 350 to 950 °C in an open furnace. The so obtained NP samples were analyzed by XRD and labeled on the basis of the respective estimated crystallite size. The nomenclature and the synthesis route of the different NP samples are reported in detail in Table 1.

Considering that the sample Ce_2 experienced damages due to the exposure to the beam during the HERFD-XANES measurement, this compound has been discarded from this discussion on the oxidation state determination and on the electronic structure. Further details on this phenomenon are provided in the Supporting Information Figure S2.

Transmission Electron Microscopy. TEM studies were performed using an aberration (image) corrected FEI Titan 80–300 operated at 300 kV providing a nominal information limit of 0.8 Å in TEM mode and a resolution of 1.4 Å in STEM mode. TEM micrographs have been recorded using a Gatan US1000 slowscan CCD camera, while STEM images have been recorded using a Fischione high-angle annular dark-field (HAADF) detector with a camera length of 195 mm. The samples for analysis have been prepared by dropping coating with a suspension of the NPs in ultrapure water on carbon-coated copper grids.

Fourier Transform Infrared Spectroscopy. Dehydrated ceria NPs were analyzed by FTIR in attenuated total reflectance mode with an Alpha Platinum Bruker spectrometer equipped with ZnSe crystal. FTIR spectra were obtained at room temperature in the wavenumber range from 600 to 4000 cm^{-1} with a resolution of 4 cm^{-1} .

Thermogravimetric Analysis. The thermal behavior of ceria NPs was investigated using a Netzsch STA 449C DTA/TG using an alumina crucible and in air atmosphere. The temperature was controlled by a Pt–PtRh (10%) thermocouple. Measurements were carried out at constant heating and cooling rates of 10 °C/min between 40 and 700 °C.

Raman. Raman measurements of nanocrystalline samples were performed at room temperature with a Horiba Jobin-Yvon T64000 spectrometer using a Kr+ laser with excitation wavelength of 647 nm. A 50 \times objective was used to irradiate powder samples and collect the backscattered light. The analyses were performed with an incident laser power in the 4–10 mW; no effect of laser power was observed for the resulting spectra in this range.

Table 1. Synthesis Route, Particle Size, and Lattice Parameter^a

sample name	synthesis route	crystallite size (nm) ^b	lattice parameter (Å) ^b	strain (%) ^b
Ce_2	hydrothermal treatment of Ce(IV) hydroxide (3h at 150 °C under autogenic pressure)	2.0 ± 0.1	5.456(3)	0.041
Ce_5.6	hydrothermal treatment of Ce(IV) hydroxide (3h at 200 °C under autogenic pressure)	5.6 ± 0.4	5.415(1)	0.015
Ce_8.4	Ce_2 heated 1h at 350 °C in air	8.4 ± 0.9	5.413(2)	0.011
Ce_12.2	Ce_4.2 ^c heated 1h at 500 °C in air	12.2 ± 1.5	5.412(1)	0.008
Ce_18.2	Ce_4.2 ^c heated 1h at 700 °C in air	18.2 ± 1.4	5.412(1)	0.006
Ce_20.8	Ce_4.2 ^c heated 1h at 800 °C in air	20.8 ± 0.7	5.412(1)	0.005
Ce_34	Ce_4.2 ^c heated 1h at 900 °C in air	34 ± 3	5.412(1)	0.004
Ce_59	Ce_4.2 ^c heated 1h at 925 °C in air	59 ± 5	5.411(1)	0.002
Ce_91	Ce_4.2 ^c heated 1h at 950 °C in air	91 ± 12	5.411(1)	0.001

^aNote that Ce_2 was measured by HERFD-XANES, but the results are not presented here due to the beam damage. ^bDerived from the refinement of the XRD patterns. ^cCe_4.2 nanopowder was synthesized by hydrothermal treatment of Ce(IV) hydroxide (3 h at 180 °C under autogenic pressure). The particle size of Ce_4.2 was estimated to be 4.2 ± 0.3 nm from the XRD pattern.

X-ray Photoelectron Spectroscopy. XPS measurements were performed with a Physical Electronics Quantera Scanning X-ray Microprobe. This system uses a focused monochromatic Al K α X-ray (1486.7 eV) source for excitation and a spherical section analyzer. The instrument has a 32 element multichannel detection system. The X-ray beam is incident normal to the sample, and the photoelectron detector is at 45° off-normal. High-energy resolution spectra were collected using a pass energy of 69.0 eV with a step size of 0.125 eV. For the Ag 3d_{5/2} line, these conditions produced a full width at half-maximum (fwhm) of 0.92 eV ± 0.05 eV. The binding energy (BE) scale is calibrated using the Cu 2p_{3/2} feature at 932.62 ± 0.05 eV and Au 4f_{7/2} at 83.96 ± 0.05 eV. The sample experienced variable degrees of charging. Low-energy electrons at ~1 eV, 20 μ A and low-energy Ar⁺ ions were used to minimize this charging. The binding energy scale was charge corrected referencing the Ce 3d_{3/2}4f⁰ (u''') line at 916.7 eV.^{16,17} The quantification and peak fitting were performed using PHI MultiPak version 9.6.1.7 software, where the experimental results were fitted to 10 peaks, defined as v⁰, v, v', v'', v''', u⁰, u, u', u'', and u'''.¹⁶ In this scheme, v, v', v'', u, u', and u''' were associated with Ce^{IV}, while v⁰, v', u⁰, and u' were associated with Ce^{III}. The relative areas of the fitted peaks were measured in order to determine the relative concentration in the surface.

High-Energy Resolution Fluorescence-Detected X-ray Absorption Near Edge Structure. HERFD-XANES measurements were conducted at the CAT-ACT beamline (ACT station) of the KIT synchrotron light source (Karlsruhe Institute of Technology, Karlsruhe, Germany).^{18,19} The incident energy was selected using the (111) reflection of a double Si crystal monochromator. The X-ray beam was focused to 500 × 500 μ m onto the sample. XANES spectra were measured in HERFD mode using an X-ray emission spectrometer.^{12,19} The sample, analyzer crystal, and a single diode VITUS Silicon Drift Detector (KETEK, Germany) were arranged in a vertical Rowland geometry. The Ce HERFD-XAS spectra at the L_{III} edge were obtained by recording the maximum intensity of the Ce L α_1 emission line (4839 eV) as a function of the incident energy. The emission energy was selected using the \langle 331 \rangle reflection of four

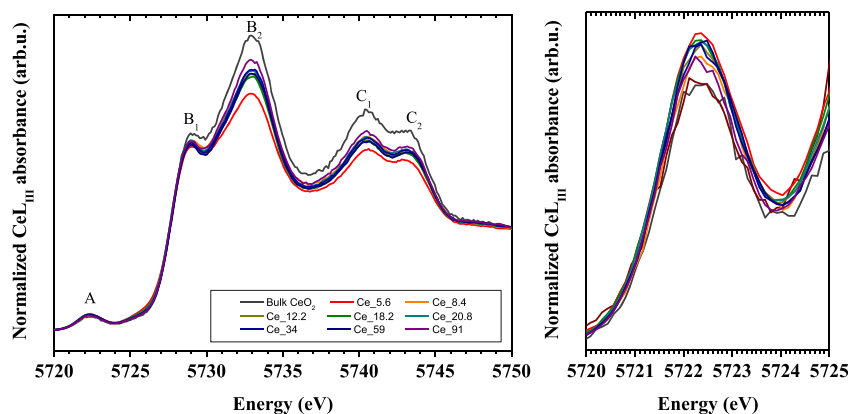


Figure 1. (Left) Ce L_3 HERFD-XANES spectra of CeO_2 NPs with different sizes compared to bulk CeO_2 (>100 nm). (Right) Pre-edge region of the Ce L_3 HERFD-XANES spectra.

spherically bent Ge crystal analyzer (with a bending radius $R = 1$ m) aligned at a 80.7° Bragg angle. The experimental energy resolution was 1.15 eV obtained by measuring the fwhm of the elastically scattered incident beam with an energy of 4.8404 keV. During the measurements, a slit with the dimensions $500 \times 500 \mu\text{m}$ was used in front of the sample, cutting of tails in the profile of the incident beam. This potentially led to a slight improvement of the experimental resolution, that is, 1 eV (it is an estimation). The experimental resolution measured at ID26, ESRF using the same analyzer crystals was 0.9 eV.²⁰ The sample, crystals, and detector were confined in a box filled with He, and a constant He flow was maintained in order to minimize the loss of intensity due to absorption and scattering of the X-rays. The data were not corrected for self-absorption effects. The sample exposure to the beam was minimized to account for possible beam damage and checked by first collecting short XANES scans (~ 10 s) to look for irradiation effect.

Theoretical Calculations. The spectra of bulk CeO_2 and CeO_2 in 2 nm were performed in a manner described in refs 21–24 using the FEFF 9.6. code. Similar to the work of Li et al. and Plakhova et al., we show here only part of the absorption spectra, which corresponds to the $2p$ – $5d$ transitions, and omit multielectron excitations from the experimental data, which appear at higher incident energy.

RESULTS AND DISCUSSION

Ce Valence in the As-Synthesized CeO_2 NPs. Our XRD and TEM data (Supporting Information Figures S3 and S4) show that the as-synthesized CeO_2 NPs crystallize in the $Fm\bar{3}m$ fluorite structure (space group 225). Depending on the experimental conditions (and particularly the annealing temperature), the average crystallite diameters vary from 2.0 ± 0.1 to 91 ± 12 nm. These XRD-refined parameters are gathered in the Table 1 and will be more thoroughly discussed in a following section.

The oxidation state and electronic structure of Ce was assessed using Ce L_{III} edge HERFD-XANES and XPS, which corresponding spectra are respectively given in Figures 1 and 2.

The HERFD-XANES spectra of all the investigated CeO_2 NPs exhibit a single pre-edge peak aligned with that of the bulk- CeO_2 reference spectrum. This pre-edge peak (noted A in Figure 1) originates from the $2p$ transition to a mixed $5d$ – $4f$ valence state^{22,25} and is characteristic of the Ce valence of the probed sample. Indeed, a single peak is observed in the pre-edge region of a pure Ce^{IV} compound, since the photoabsorption process excites an electron to the $4f$ level, formally empty in the initial state. However, in the case of a Ce^{III} ion, the interaction between the $4f$ electron in the initial state and the second electron excited by the photon leads to a splitting of

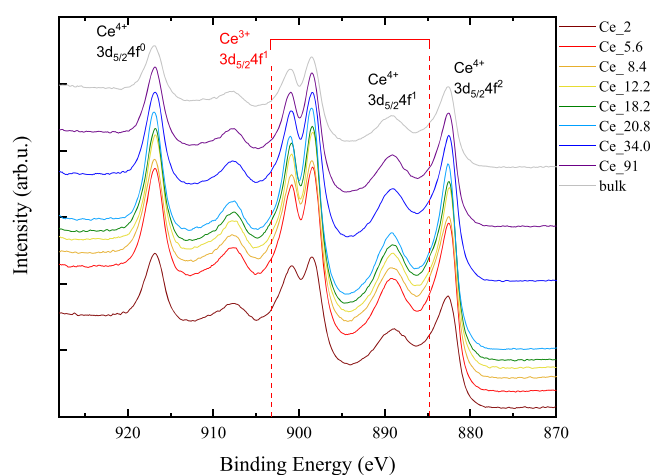


Figure 2. High-energy resolution photoemission spectra of the Ce 3d spectral region. The spectra confirm the presence of the dominating Ce^{IV} .

the pre-edge feature into two groups of transition, whose energy position is related to the electron–electron interactions in the $4f$ level.^{20,26,27} Consequently, the pre-edge structure of the NPs reveals solely the presence of Ce in the IV oxidation state. Additionally, since XANES is extremely sensitive to the local structure, those similarities corroborate our XRD findings that CeO_2 NPs all crystallize in the same space group.⁸

Regarding our XPS results, Figure 2 provides the Ce $3d_{3/2,5/2}$ XPS spectra collected for the CeO_2 NPs. The spectra of CeO_2 are composed of 6 peaks corresponding 3 doublets belonging to $3d_{3/2}$ and $3d_{5/2}$ core holes spin–orbit splitting. The highest energy peaks, u''' at 916.7 eV and v''' at 898.2 eV, are the doublet from the ejection with the Ce $3d_{3/2}4f^0$ final state. The next doublet, u'' at 907.4 eV and v'' at 888.8 eV, are the result of Ce $3d_{5/2}4f^1$, followed by u at 900.8 eV and v at 882.4 eV, corresponding to the result of a Ce $3d_{5/2}4f^2$ final state. All of these multiplets are associated with Ce^{IV} , which are consistent with previously published CeO_2 reference XPS data. On the other hand, the Ce 3d XPS spectrum of $\text{Ce}^{III}\text{PO}_4$ ref 28 has two distinct sets of doublets: v^0 at 880.6 eV and u^0 at 897.9 eV as a result of Ce $3d_{5/2}4f^2$ ejection, and v' at 884.5 eV and u' at 900.8 eV as a result of the Ce $3d_{5/2}4f^1$ final state, neither of which register a meaningful peak area in this data. Furthermore, from the peak fitting performed (Supporting Information Figure S5), no characteristic band feature of Ce^{III}

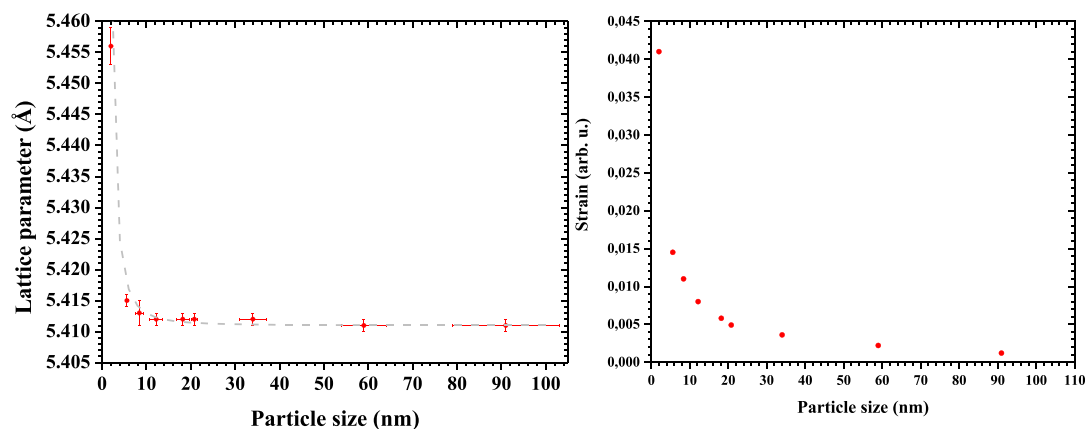


Figure 3. Decrease of both lattice parameter (left) and strain (right) with the particle size. The lattice parameter, the strain, and the particle size have been calculated from the Rietveld refinement of the corresponding XRD patterns. All the values are provided in Table 1 of the Supporting Information. The gray dotted line corresponds to the power-law relation proposed by Baranchikov et al.³¹ The goodness of fit was 0.963.

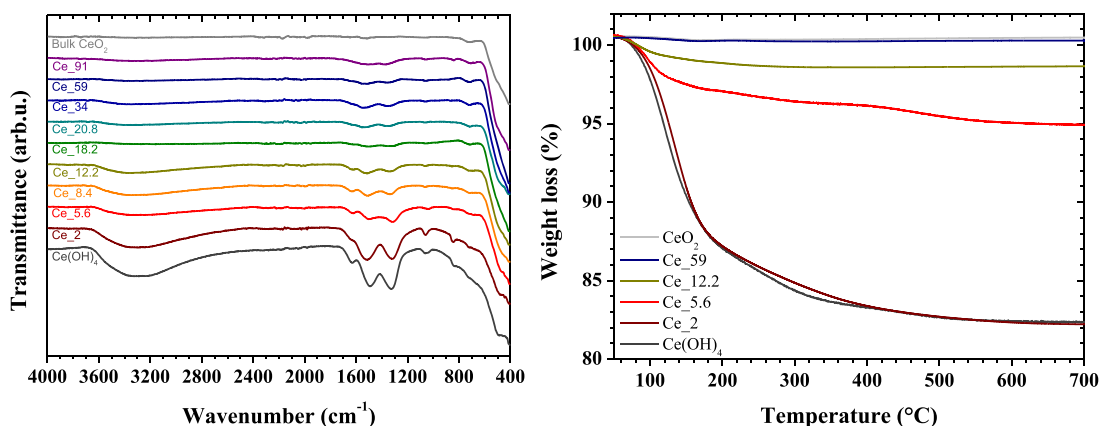


Figure 4. Determination of the adsorbed surface species. (Left) FTIR spectra of CeO₂ NPs compared with Ce(OH)₄ and bulk-CeO₂ references. (Right) TGA data of CeO₂ NPs of different sizes compared with Ce(OH)₄ and bulk-CeO₂.

was found for samples across all crystallite sizes, corroborating the XANES findings that only tetravalent cerium is present.

Size Dependence of the Lattice Parameter. The unit cell parameter variation as a function of the NPs' size has been reported for several oxide NPs, including ThO₂, CeO₂, MgO, Co₃O₄, Fe₃O₄, TiO₂, etc., but remains a subject of discussion.^{2,29–35}

Figure 3 presents the size dependence of the lattice parameters of the as-synthesized CeO₂ NPs. When the particle size changes from 2.0 to 91 nm, the unit cell value varies from 5.456 (3) to 5.411 (1) Å. Note that the latter value corresponds to bulk CeO₂. In our work and as already reported for CeO₂-based NPs,^{32,36,2,31} noticeable deviation of the lattice parameter can be observed for particles which sizes are smaller than ca. 5 nm. The collected data can be adequately fitted using a power-law relation proposed by Baranchikov et al.³¹

According to the paper of Diehm et al.,³⁷ which gathers a large body of experimental data and theoretical calculation, two main models have been proposed to explain this lattice parameter variation. Tsunekawa et al. argued that the unit cell is affected by the formation of oxygen vacancies in the smaller NPs, which leads to a change in the oxidation state of the constituting cation. The second model, which is most commonly admitted, attributes the variation to the surface stress resulting from the difference of coordination between

atoms on the surface and in the bulk.^{9,10} This effect becomes more pronounced as the particle size reduces, that is, as the contribution of the surface atoms to the structural characteristics increases. From our HERFD-XANES and XPS findings, the presence of Ce^{III} and hence of the oxygen vacancy has been discarded, which means that the observed lattice expansion might then be only due to surface stress. To corroborate this assumption, the formation of species present at the NPs surface has been studied by FTIR and TGA measurements. Each FTIR spectrum (Figure 4) shows an absorption band at ca. 450 cm⁻¹ characteristic of the CeO₂ stretching vibration. Some bands are also visible in the 1300–1700 cm⁻¹ region and may be assigned to C–H bending and stretching of C–O bond. The latter may be caused by adsorbed CO₂ or contamination with ethanol during the synthesis procedure. The signal at 1630 cm⁻¹ is associated with the bending frequency of molecular H₂O (H–O–H). The broad adsorption band at ca. 3400 cm⁻¹ corresponds to hydrated and physically adsorbed water in the sample.^{9,38,39} Recently, TGA coupled with mass spectrometry measurement, performed on ThO₂ NPs, has shown that H₂O and CO₂ were adsorbed on the NPs surfaces. The corresponding molar fractions of H₂O and CO₂ were inversely proportional to the NPs size.⁴⁰ Similar observation was obtained from our TGA data presented in the Figure 4. Ce₂ and Ce₅₉ have similar thermal decompositions as Ce(OH)₄ and CeO₂, respectively,

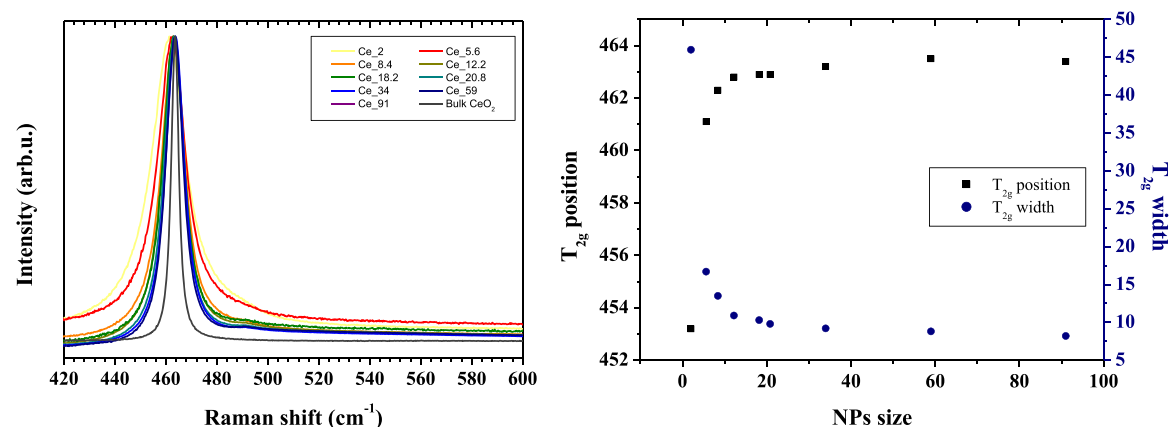


Figure 5. (Left) Raman spectra. (Right) T_{2g} position and width as a function of the particle size.

while Ce_5.6 and Ce_12.2 exhibit intermediates weight losses. The thermal decompositions of these later are clearly composed of three-well-defined steps. The first decomposition step (step I) is observed at 25–180 °C. The second weight loss (step II) occurs at 180–350 °C. The third decomposition step (step III) occurs at 350–700 °C. Our TGA data shows that the weight loss is proportional to the surface to volume ratio, suggesting a higher concentration of adsorbed species on the smaller NPs.

The Raman spectrum of bulk CeO_2 shows one Raman active fundamental mode at 464 cm^{-1} (Figure 5). This band corresponds to the triply degenerate T_{2g} Raman active mode of the O_h point group and is due to the stretching of the O–O bond. Comparison with the CeO_2 NPs reveals a red-shift and an asymmetrical broadening if the T_{2g} mode with decreasing NPs size. Both T_{2g} position and width were fitted and plotted in Figure 5. It can be seen that an increase of the NPs size induces an increase of the T_{2g} position and a decrease of the T_{2g} width. Similar observations have already been reported for CeO_2 and other nanocrystals.^{41–43} Several factors can contribute to the changes in the Raman peak position and line width of the T_{2g} peak with NP size. These include phonon confinement, strain, broadening associated with the size distribution, defects, and surface effect.^{41–46} In most studies, the red shift is majorly attributed to the lattice expansion and associated strain that occurs when oxygen vacancies are created, which leads to the reduction of Ce^{IV} (ionic radius 0.970 \AA)⁴⁷ in Ce^{III} (ionic radius 1.143 \AA).⁴⁷ However, the creation of O vacancies and the reduction of Ce^{IV} in Ce^{III} induce a local symmetry distortion, and new Raman bands located around 550 and 595 cm^{-1} are observed.⁴⁸ The absence of both new Raman bands and detection of Ce^{III} from our HERFD-XANES measurements allows us to discard this hypothesis for the T_{2g} red-shift. One possible explanation could be that the stress generated by the presence of the adsorbed species at the NPs surface would enhance the downward shift and broadening of the T_{2g} .

Size Dependence of the Electronic Structure. The HERFD-XANES spectrum of bulk CeO_2 exhibits three characteristic features A, B, and C with a doublet structure for B and C leading to a total of five bands indicated by A, B_1 , B_2 , C_1 , and C_2 in Figure 1. The pre-edge peak (noted A) originates from the dipole-forbidden $2p$ transition to a mixed $5d$ – $4f$ valence state, while the B and C arises from transitions from $2p_{3/2} \rightarrow 5d_{5/2}$ states. The splitting of B_1 and C_1 into a doublet structure is due to the crystal field splitting of $5d$

states.⁴⁹ These edge features have been assigned to screened (B_1 and B_2) and unscreened (C_1 and C_2) excited states.^{22,50} B_1 and B_2 features described the $2p \rightarrow 5d$ transition with $4f^1L$ configuration, while C_1 and C_2 are representatives of the $2p \rightarrow 5d$ transition from $4f^0L$ configuration, where L corresponds to the orbital angular momentum.^{23,51} In the CeO_2 fluorite structure, each Ce atom is surrounded by 8 oxygen atoms located at the corners of a cube creating a cubic crystal field belonging to the O_h point symmetry group. Due to this cubic crystal field, the $\text{Ce}^{\text{IV}} 5d^0$ configuration is split into the e_g and t_{2g} bands corresponding to B_1 , C_2 and B_2 , C_1 , respectively.^{23,52} The Ce^{IV} valence corresponds to a $5d^0$ configuration, implying that in the HERFD-XANES process, t_{2g} is first filled with electrons, while the e_g is empty as the transferred energy is not sufficient. Here the experimental crystal-field energy splitting of Ce $5d$ in bulk CeO_2 is ca. 4 eV . This value of energy gap between e_g and t_{2g} is in good agreement with previously published values.^{53–55}

Now, looking at the experimental HERFD-XANES spectra of CeO_2 NPs, one can observe that all the A, B_1 , B_2 , C_1 , and C_2 features are presented at the same energy position as in bulk CeO_2 . A value of ca. 4 eV is found for the experimental crystal-field energy splitting of Ce $5d$ in bulk CeO_2 NPs, indicating that this energy gap is not affected by the particle size. However, one can note that the e_g feature intensity remains constant for both NPs and bulk CeO_2 , while the t_{2g} intensity is proportional to the particle size. This experimental observation is corroborated by our theoretical calculations, showing that the simulated HERFD-XANES spectra of 2 nm CeO_2 exhibit a t_{2g} intensity smaller than that of bulk CeO_2 . The stability of the e_g feature is also well reproduced. One possible explanation lies in the presence of adsorbed species at the NPs surfaces. In the case of bulk CeO_2 , the corresponding HERFD-XANES spectra are a direct measurement of the electronic structure of bulk Ce atoms. However, in the case of our NPs, the measured spectra correspond to the average electronic structure of both Ce atoms in the bulk and at the surface. This implies that the observed t_{2g} variation originates from the electronic structure of surface Ce atoms. We showed in the previous section that Ce remains in the IV oxidation state and that the fraction of adsorbed species is inversely proportional to the particle size. In other words, their content is increasing with the surface Ce atoms to bulk Ce atoms ratio. Considering that the e_g level is empty in $\text{Ce } 5d^0$, the bonding between the surface Ce atoms and the adsorbed species requires the delocalization of the t_{2g} electrons, hence explaining the observed decrease of the t_{2g}

intensity on the Ce L_{III} HERFD-XANES spectra. One can also assume that this bonding affects the crystal field by creating new d levels. This larger degeneracy of the t_{2g} level is clearly observable for the sample Ce_5.6 which exhibits a broader t_{2g} feature (Figure 6).

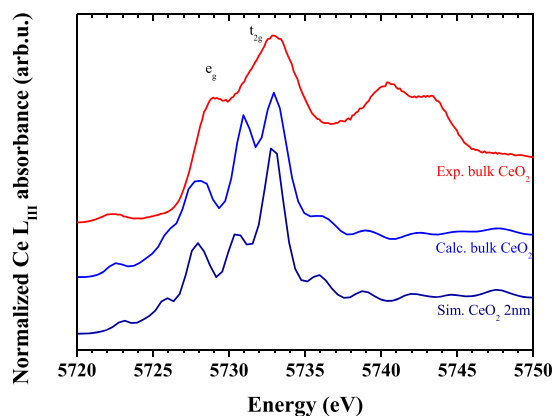


Figure 6. Comparison of experimental and calculated Ce L_{III} HERFD-XANES spectra of both 2 nm CeO_2 and bulk CeO_2 . Calculated data shown here are reproduced from Plakhova et al.²¹ Theoretical calculations predict a lower t_{2g} intensity for the 2 nm CeO_2 .

The effect of the NPs size and the presence of adsorbed surface groups on the shape of the Ce L_3 HERFD-XANES spectrum has been previously discussed by Plakhova et al.²¹ The CeO_2 NPs investigated here were made by hydrothermal treatment at a temperature above 500 °C, which limits the availability of the adsorbed species at the surface and allows showing the effect of the particle size on the crystal field splitting of the Ce 5d states, which, to our knowledge, is shown here for the first time.

CONCLUSION

In this work, we have synthesized fluorite $Ce^{IV}O_2$ NPs and studied the effect of the NP size on both local and electronic structure. By analogy with other metal oxides, we have shown that the lattice parameter expands with decreasing particle size. The presence of mainly Ce^{IV} , demonstrated by XPS and HERFD-XANES, indicates that the unit cell size dependence is not linked to the Ce valence, but to surface stress. Indeed, our TGA and FTIR data confirm the presence of surface hydroxyl and carbonate groups that have a tensile effect on the crystalline lattice. Additionally, the size dependence of the electronic structure, and especially of the t_{2g} feature in the Ce L_{III} XANES spectrum, has been experimentally evidenced and confirmed with theoretical calculations.

ASSOCIATED CONTENT

Supporting Information

The Supporting Information is available free of charge at <https://pubs.acs.org/doi/10.1021/acs.inorgchem.0c00506>.

Additional information includes sample characterizations by HEFRD-XANES, XRD, radiation damage study and TEM (PDF)

AUTHOR INFORMATION

Corresponding Authors

Damien Prieur – Helmholtz Zentrum Dresden-Rossendorf (HZDR), Institute of Resource Ecology, 01314 Dresden, Germany; The Rossendorf Beamline at ESRF–The European Synchrotron, 38043 Grenoble, Cedex 9, France; orcid.org/0000-0001-5087-0133; Email: d.prieur@hzdr.de

Walter Bonani – European Commission, Joint Research Centre, D-76125 Karlsruhe, Germany; Email: walter.bonani@ec.europa.eu

Authors

Karin Popa – European Commission, Joint Research Centre, D-76125 Karlsruhe, Germany

Olaf Walter – European Commission, Joint Research Centre, D-76125 Karlsruhe, Germany; orcid.org/0000-0002-2679-1715

Kyle W. Kriegsman – Department of Chemistry and Alexandra Navrotsky Institute for Experimental Thermodynamics, Washington State University, Pullman, Washington 99164, United States

Mark H. Engelhard – Environmental Molecular Sciences Laboratory, Pacific Northwest National Lab, Richland, Washington 99352, United States; orcid.org/0000-0002-5543-0812

Xiaofeng Guo – Department of Chemistry and Alexandra Navrotsky Institute for Experimental Thermodynamics, Washington State University, Pullman, Washington 99164, United States; orcid.org/0000-0003-3129-493X

Rachel Eloirdi – European Commission, Joint Research Centre, D-76125 Karlsruhe, Germany

Thomas Gouder – European Commission, Joint Research Centre, D-76125 Karlsruhe, Germany

Aaron Beck – Institute for Nuclear Waste Disposal, Karlsruhe Institute of Technology, 76021 Karlsruhe, Germany

Tonya Vitova – Institute for Nuclear Waste Disposal, Karlsruhe Institute of Technology, 76021 Karlsruhe, Germany;

orcid.org/0000-0002-3117-7701

Andreas C. Scheinost – Helmholtz Zentrum Dresden-Rossendorf (HZDR), Institute of Resource Ecology, 01314 Dresden, Germany; The Rossendorf Beamline at ESRF–The European Synchrotron, 38043 Grenoble, Cedex 9, France; orcid.org/0000-0002-6608-5428

Kristina Kvashnina – Helmholtz Zentrum Dresden-Rossendorf (HZDR), Institute of Resource Ecology, 01314 Dresden, Germany; The Rossendorf Beamline at ESRF–The European Synchrotron, 38043 Grenoble, Cedex 9, France

Philippe Martin – CEA, DEN, DMRC, SFMA, LCC, F30207 Bagnols sur Cèze, France

Complete contact information is available at:

<https://pubs.acs.org/10.1021/acs.inorgchem.0c00506>

Author Contributions

K.P. and O.W. carried out the NPs synthesis work. W.B., K.P., and O.W. performed characterizations of the samples using in-house laboratory equipment. D.P. and P.M. performed synchrotrons measurements and associated data treatment. A.B. and T.V. set up the spectrometer for U M4 measurements. K.W.K., M.H.E., X.G., R.E., and T.G. did the XPS measurements. K.O.K. did the theoretical simulation of the experimental spectra. D.P., W.B., K.P., and P.M. cowrote the paper. D.P., W.B., K.P., P.M., O.W., and A.C.S. were involved

in planning and supervision of the work. All authors discussed the results and contributed to the final manuscript.

Notes

The authors declare no competing financial interest.

ACKNOWLEDGMENTS

D.P., K.P., and W.B. acknowledge the KIT light source for provision of instruments at their beamlines and the Institute for Beam Physics and Technology (IBPT) for the operation of the storage ring, the Karlsruhe Research Accelerator (KARA). D.P., K.P., and W.B. are thankful to Dr. Kathy Dardenne and Dr. Joerg Rothe for their help during the beamtime. D.P. is also indebted to the ID26 team that lent us the crystals for XAS measurements. In addition, K.P., W.B., and O.W. acknowledge Sarah Stöhr and Herwin Hein for the technical support and TGA and Dr. Heike Störmer from the Laboratory for Electron Microscopy of the Karlsruhe Institute of Technology (KIT) for TEM images. X.G. and K.W.K. acknowledge the institutional funds from the Department of Chemistry at Washington State University (WSU) and the support by the U.S. Department of Energy, Office of Nuclear Energy, grant DE-NE0008582. A portion of this research was performed using EMSL (grid.436923.9), a DOE Office of Science User Facility sponsored by the Office of Biological and Environmental Research. K.O.K. acknowledges support from European Research Council (grant no. 75969).

REFERENCES

- (1) Trovarelli, A. Catalytic Properties of Ceria and CeO₂-Containing Materials. *Catal. Rev.: Sci. Eng.* **1996**, *38* (4), 439–520.
- (2) Montini, T.; Melchionna, M.; Monai, M.; Fornasiero, P. Fundamentals and Catalytic Applications of CeO₂-Based Materials. *Chem. Rev.* **2016**, *116* (10), 5987–6041.
- (3) Ma, L.; Chen, R.; Zhu, G.; Hu, Y.; Wang, Y.; Chen, T.; Liu, J.; Jin, Z. Cerium Oxide Nanocrystal Embedded Bimodal Microporous Nitrogen-Rich Carbon Nanospheres as Effective Sulfur Host for Lithium–Sulfur Batteries. *ACS Nano* **2017**, *11* (7), 7274–7283.
- (4) Li, P.; Chen, X.; Li, Y.; Schwank, J. W. A Review on Oxygen Storage Capacity of CeO₂-Based Materials: Influence Factors, Measurement Techniques, and Applications in Reactions Related to Catalytic Automotive Emissions Control. *Catal. Today* **2019**, *327*, 90–115.
- (5) Dhall, A.; Self, W. Cerium Oxide Nanoparticles: A Brief Review of Their Synthesis Methods and Biomedical Applications. *Antioxidants* **2018**, *7* (8), 97.
- (6) Kim, H. S.; Joung, C. Y.; Lee, B. H.; Oh, J. Y.; Koo, Y. H.; Heimgartner, P. Applicability of CeO₂ as a Surrogate for PuO₂ in a MOX Fuel Development. *J. Nucl. Mater.* **2008**, *378* (1), 98–104.
- (7) Adekoya, J. A.; Ogunniran, K. O.; Siyanbola, T. O.; Dare, E. O.; Revaprasadu, N. Band Structure, Morphology, Functionality, and Size-Dependent Properties of Metal Nanoparticles. *Noble and Precious Metals - Properties, Nanoscale Effects and Applications*; Intech: Rijeka, Croatia, 2018. DOI: 10.5772/intechopen.72761
- (8) Amidani, L.; Plakhova, T. V.; Romanchuk, A. Y.; Gerber, E.; Weiss, S.; Efimenko, A.; Sahle, C. J.; Butorin, S. M.; Kalmykov, S. N.; Kvashnina, K. O. Understanding the Size Effects on the Electronic Structure of ThO₂ Nanoparticles. *Phys. Chem. Chem. Phys.* **2019**, *21* (20), 10635–10643.
- (9) Wu, N.-C.; Shi, E.-W.; Zheng, Y.-Q.; Li, W.-J. Effect of PH of Medium on Hydrothermal Synthesis of Nanocrystalline Cerium(IV) Oxide Powders. *J. Am. Ceram. Soc.* **2002**, *85* (10), 2462–2468.
- (10) Wang, Y.-J.; Dong, H.; Lyu, G.-M.; Zhang, H.-Y.; Ke, J.; Kang, L.-Q.; Teng, J.-L.; Sun, L.-D.; Si, R.; Zhang, J.; Liu, Y.-J.; Zhang, Y.-W.; Huang, Y.-H.; Yan, C.-H. Engineering the Defect State and Reducibility of Ceria Based Nanoparticles for Improved Anti-Oxidation Performance. *Nanoscale* **2015**, *7* (33), 13981–13990.
- (11) Batuk, O. N.; Szabó, D. V.; Denecke, M. A.; Vitova, T.; Kalmykov, S. N. Synthesis and Characterization of Thorium, Uranium and Cerium Oxide Nanoparticles. *Radiochimica Acta International journal for chemical aspects of nuclear science and technology* **2013**, *101* (4), 233–240.
- (12) Glatzel, P.; Bergmann, U. High Resolution 1s Core Hole X-Ray Spectroscopy in 3d Transition Metal Complexes—Electronic and Structural Information. *Coord. Chem. Rev.* **2005**, *249* (1), 65–95.
- (13) Prieur, D.; Martel, L.; Vigier, J.-F.; Scheinost, A. C.; Kvashnina, K. O.; Somers, J.; Martin, P. M. Alivalent Cation Substitution in UO₂: Electronic and Local Structures of U1–YLaYO₂ ± x Solid Solutions. *Inorg. Chem.* **2018**, *57* (3), 1535–1544.
- (14) Balice, L.; Bouëxière, D.; Cologna, M.; Cambriani, A.; Vigier, J.-F.; De Bona, E.; Sorarù, G. D.; Kübel, C.; Walter, O.; Popa, K. Nano and Micro U1–XThxO₂ Solid Solutions: From Powders to Pellets. *J. Nucl. Mater.* **2018**, *498*, 307–313.
- (15) Vălu, S.-O.; De Bona, E.; Popa, K.; Griveau, J.-C.; Colineau, E.; Konings, R. J. M. The Effect of Lattice Disorder on the Low-Temperature Heat Capacity of (U 1-y Th y)O₂ and 238 Pu-Doped UO₂. *Sci. Rep.* **2019**, *9* (1), 15082.
- (16) Paparazzo, E. Use and Mis-Use of x-Ray Photoemission Spectroscopy Ce3d Spectra of Ce₂O₃ and CeO₂. *J. Phys.: Condens. Matter* **2018**, *30* (34), 343003.
- (17) Eloidri, R.; Cakir, P.; Huber, F.; Seibert, A.; Konings, R.; Gouder, T. X-Ray Photoelectron Spectroscopy Study of the Reduction and Oxidation of Uranium and Cerium Single Oxide Compared to (U-Ce) Mixed Oxide Films. *Appl. Surf. Sci.* **2018**, *457*, 566–571.
- (18) Zimina, A.; Dardenne, K.; Denecke, M. A.; Grunwaldt, J. D.; Huttel, E.; Lichtenberg, H.; Mangold, S.; Pruessmann, T.; Rothe, J.; Steininger, R.; Vitova, T. The CAT-ACT Beamline at ANKA: A New High Energy X-Ray Spectroscopy Facility for CATALysis and ACTinide Research. *J. Phys.: Conf. Ser.* **2016**, *712*, 012019.
- (19) Zimina, A.; Dardenne, K.; Denecke, M. A.; Doronkin, D. E.; Huttel, E.; Lichtenberg, H.; Mangold, S.; Pruessmann, T.; Rothe, J.; Spangenberg, Th.; Steininger, R.; Vitova, T.; Geckeis, H.; Grunwaldt, J.-D. CAT-ACT—A New Highly Versatile x-Ray Spectroscopy Beamline for Catalysis and Radionuclide Science at the KIT Synchrotron Light Facility ANKA. *Rev. Sci. Instrum.* **2017**, *88* (11), 113113.
- (20) Cafun, J.-D.; Kvashnina, K. O.; Casals, E.; Puentes, V. F.; Glatzel, P. Absence of Ce³⁺ Sites in Chemically Active Colloidal Ceria Nanoparticles. *ACS Nano* **2013**, *7* (12), 10726–10732.
- (21) Plakhova, T. V.; Romanchuk, A. Y.; Butorin, S. M.; Konyukhova, A. D.; Egorov, A. V.; Shiryayev, A. A.; Baranchikov, A. E.; Dorovatovskii, P. V.; Huthwelker, T.; Gerber, E.; Bauters, S.; Sozarukova, M. M.; Scheinost, A. C.; Ivanov, V. K.; Kalmykov, S. N.; Kvashnina, K. O. Towards the Surface Hydroxyl Species in CeO₂ Nanoparticles. *Nanoscale* **2019**, *11*, 18142.
- (22) Soldatov, A. V.; Ivanchenko, T. S.; Kotani, A.; Bianconi, A. L₃ Edge X-Ray Absorption Spectrum of CeO₂: Crystal Structure Effects. *Phys. B* **1995**, *208–209*, 53–55.
- (23) Kotani, A.; Kvashnina, K. O.; Butorin, S. M.; Glatzel, P. Spectator and Participant Processes in the Resonant Photon-in and Photon-out Spectra at the Ce L₃ Edge of CeO₂. *Eur. Phys. J. B* **2012**, *85* (8), 257.
- (24) Li, Y.; Kraynis, O.; Kas, J.; Weng, T.-C.; Sokaras, D.; Zacharowicz, R.; Lubomirsky, I.; Frenkel, A. I. Geometry of Electromechanically Active Structures in Gadolinium - Doped Cerium Oxides. *AIP Adv.* **2016**, *6* (5), 055320.
- (25) Kvashnina, K. O.; Butorin, S. M.; Glatzel, P. Direct Study of the F-Electron Configuration in Lanthanide Systems. *J. Anal. At. Spectrom.* **2011**, *26* (6), 1265–1272.
- (26) Safonova, O. V.; Guda, A. A.; Paun, C.; Smolentsev, N.; Abdala, P. M.; Smolentsev, G.; Nachttegaal, M.; Szlachetko, J.; Soldatov, M. A.; Soldatov, A. V.; van Bokhoven, J. A. Electronic and Geometric Structure of Ce³⁺ Forming Under Reducing Conditions in Shaped

Ceria Nanoparticles Promoted by Platinum. *J. Phys. Chem. C* **2014**, *118* (4), 1974–1982.

(27) Gasperi, G.; Amidani, L.; Benedetti, F.; Boscherini, F.; Glatzel, P.; Valeri, S.; Luches, P. Electronic Properties of Epitaxial Cerium Oxide Films during Controlled Reduction and Oxidation Studied by Resonant Inelastic X-Ray Scattering. *Phys. Chem. Chem. Phys.* **2016**, *18* (30), 20511–20517.

(28) Bêche, E.; Charvin, P.; Perarnau, D.; Abanades, S.; Flamant, G. Ce 3d XPS Investigation of Cerium Oxides and Mixed Cerium Oxide (Ce_xTi_{1-x}O₂). *Surf. Interface Anal.* **2008**, *40* (3–4), 264–267.

(29) Swamy, V.; Menzies, D.; Muddle, B. C.; Kuznetsov, A.; Dubrovinsky, L. S.; Dai, Q.; Dmitriev, V. Nonlinear Size Dependence of Anatase TiO₂ Lattice Parameters. *Appl. Phys. Lett.* **2006**, *88* (24), 243103.

(30) Cimino, A.; Porta, P.; Valigi, M. Dependence of the Lattice Parameter of Magnesium Oxide on Crystallite Size. *J. Am. Ceram. Soc.* **1966**, *49* (3), 152–156.

(31) Baranchikov, A. E.; Polezhaeva, O. S.; Ivanov, V. K.; Tretyakov, Y. D. Lattice Expansion and Oxygen Non-Stoichiometry of Nanocrystalline Ceria. *CrystEngComm* **2010**, *12* (11), 3531–3533.

(32) Tsunekawa, S.; Sahara, R.; Kawazoe, Y.; Ishikawa, K. Lattice Relaxation of Monosize CeO_{2-x} Nanocrystalline Particles. *Appl. Surf. Sci.* **1999**, *152* (1), 53–56.

(33) Hailstone, R. K.; DiFrancesco, A. G.; Leong, J. G.; Allston, T. D.; Reed, K. J. A Study of Lattice Expansion in CeO₂ Nanoparticles by Transmission Electron Microscopy. *J. Phys. Chem. C* **2009**, *113* (34), 15155–15159.

(34) Rodenbough, P. P.; Zheng, C.; Liu, Y.; Hui, C.; Xia, Y.; Ran, Z.; Hu, Y.; Chan, S.-W. Lattice Expansion in Metal Oxide Nanoparticles: MgO, Co₃O₄, & Fe₃O₄. *J. Am. Ceram. Soc.* **2017**, *100* (1), 384–392.

(35) Chen, L.; Fleming, P.; Morris, V.; Holmes, J. D.; Morris, M. A. Size-Related Lattice Parameter Changes and Surface Defects in Ceria Nanocrystals. *J. Phys. Chem. C* **2010**, *114* (30), 12909–12919.

(36) Zhang, F.; Chan, S.-W.; Spanier, J. E.; Apak, E.; Jin, Q.; Robinson, R. D.; Herman, I. P. Cerium Oxide Nanoparticles: Size-Selective Formation and Structure Analysis. *Appl. Phys. Lett.* **2002**, *80* (1), 127–129.

(37) Diehm, P. M.; Ágoston, P.; Albe, K. Size-Dependent Lattice Expansion in Nanoparticles: Reality or Anomaly? *ChemPhysChem* **2012**, *13* (10), 2443–2454.

(38) Mokkelbost, T.; Kaus, I.; Grande, T.; Einarsrud, M.-A. Combustion Synthesis and Characterization of Nanocrystalline CeO₂-Based Powders. *Chem. Mater.* **2004**, *16* (25), 5489–5494.

(39) Pautrot-D'Alençon, L.; Barboux, P.; Boilot, J.-P. Synthesis and Acid Functionalization of Cerium Oxide Nanoparticles. *J. Sol-Gel Sci. Technol.* **2006**, *39* (3), 261–267.

(40) Plakhova, T. V.; Romanchuk, A. Yu.; Likhosherstova, D. V.; Baranchikov, A. E.; Dorovatovskii, P. V.; Svetogorov, R. D.; Shatalova, T. B.; Egorova, T. B.; Trigub, A. L.; Kvashnina, K. O.; Ivanov, V. K.; Kalmykov, S. N. Size Effects in Nanocrystalline Thoria. *J. Phys. Chem. C* **2019**, *123* (37), 23167–23176.

(41) Spanier, J. E.; Robinson, R. D.; Zhang, F.; Chan, S.-W.; Herman, I. P. Size-Dependent Properties of CeO_2 Nanoparticles as Studied by Raman Scattering. *Phys. Rev. B: Condens. Matter Mater. Phys.* **2001**, *64* (24), 245407.

(42) Lee, Y.; He, G.; Akey, A. J.; Si, R.; Flytzani-Stephanopoulos, M.; Herman, I. P. Raman Analysis of Mode Softening in Nanoparticle CeO_{2-δ} and Au-CeO_{2-δ} during CO Oxidation. *J. Am. Chem. Soc.* **2011**, *133* (33), 12952–12955.

(43) Gao, Y.; Zhao, X.; Yin, P.; Gao, F. Size-Dependent Raman Shifts for Nanocrystals. *Sci. Rep.* **2016**, *6*, 20539 DOI: 10.1038/srep20539.

(44) Schilling, C.; Hofmann, A.; Hess, C.; Ganduglia-Pirovano, M. V. Raman Spectra of Polycrystalline CeO₂: A Density Functional Theory Study. *J. Phys. Chem. C* **2017**, *121* (38), 20834–20849.

(45) Korepanov, V. I.; Chan, S.-Y.; Hsu, H.-C.; Hamaguchi, H. Phonon Confinement and Size Effect in Raman Spectra of ZnO Nanoparticles. *Heliyon* **2019**, *5* (2), No. e01222.

(46) Filtschew, A.; Hofmann, K.; Hess, C. Ceria and Its Defect Structure: New Insights from a Combined Spectroscopic Approach. *J. Phys. Chem. C* **2016**, *120* (12), 6694–6703.

(47) Shannon, R. D. Revised Effective Ionic Radii and Systematic Studies of Interatomic Distances in Halides and Chalcogenides. *Acta Crystallogr., Sect. A: Cryst. Phys., Diffr., Theor. Gen. Crystallogr.* **1976**, *32* (5), 751–767.

(48) Li, H.; Zhang, P.; Li, G.; Lu, J.; Wu, Q.; Gu, Y. Stress Measurement for Nonstoichiometric Ceria Films Based on Raman Spectroscopy. *J. Alloys Compd.* **2016**, *682*, 132–137.

(49) Paun, C.; Safonova, O. V.; Szlachetko, J.; Abdala, P. M.; Nachtegaal, M.; Sa, J.; Klyemenov, E.; Cervellino, A.; Krumeich, F.; van Bokhoven, J. A. Polyhedral CeO₂ Nanoparticles: Size-Dependent Geometrical and Electronic Structure. *J. Phys. Chem. C* **2012**, *116* (13), 7312–7317.

(50) Bianconi, A.; Marcelli, A.; Dexpert, H.; Karnatak, R.; Kotani, A.; Jo, T.; Petiau, J. Specific Intermediate-Valence State of Insulating 4f Compounds Detected by L_{3} x-Ray Absorption. *Phys. Rev. B: Condens. Matter Mater. Phys.* **1987**, *35* (2), 806–812.

(51) Fonda, E.; Andreatta, D.; Colavita, P. E.; Vlaic, G. EXAFS Analysis of the L₃ Edge of Ce in CeO₂: Effects of Multi-Electron Excitations and Final-State Mixed Valence. *J. Synchrotron Radiat.* **1999**, *6* (1), 34–42.

(52) Nakamatsu, H.; Mukoyama, T. Assignment of Ce XANES Spectra for CeO₂ and CeO_{1.75} and Effect of Oxygen Vacancy. In *Advances in Quantum Chemistry*; Elsevier: Amsterdam, 2000; Vol. 37, pp 111–125. DOI: 10.1016/S0065-3276(00)37008-3.

(53) Zhang, J.; Wu, Z.; Liu, T.; Hu, T.; Wu, Z.; Ju, X. XANES Study on the Valence Transitions in Cerium Oxide Nanoparticles. *J. Synchrotron Radiat.* **2001**, *8* (2), 531–532.

(54) Soldatov, A. V.; Ivanchenko, T. S.; Della Longa, S.; Kotani, A.; Iwamoto, Y.; Bianconi, A. Crystal-Structure Effects in the Ce L₃-Edge x-Ray-Absorption Spectrum of CeO₂: Multiple-Scattering Resonances and Many-Body Final States. *Phys. Rev. B: Condens. Matter Mater. Phys.* **1994**, *50* (8), 5074–5080.

(55) Marchbank, H. R.; Clark, A. H.; Hyde, T. I.; Playford, H. Y.; Tucker, M. G.; Thompsett, D.; Fisher, J. M.; Chapman, K. W.; Beyer, K. A.; Monte, M.; Longo, A.; Sankar, G. Structure of Nano-Sized CeO₂ Materials: Combined Scattering and Spectroscopic Investigations. *ChemPhysChem* **2016**, *17* (21), 3494–3503.